


Dissociative electron attachment in NCCN: Absolute cross sections and velocity-map imagingPamir Nag,^{*} Miroslav Poláček, and Juraj Fedor[†]*J. Heyrovský Institute of Physical Chemistry, Czech Academy of Sciences, Dolejškova 3, 18223 Prague, Czech Republic* (Received 27 February 2019; revised manuscript received 9 April 2019; published 28 May 2019)

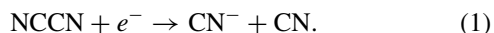
We study the CN^- production from cyanogen using an experimental setup which combines the trochoidal electron monochromator with the velocity map imaging detection spectrometer. The setup is quantitative and the absolute dissociative electron attachment cross sections are determined using the relative flow technique. The peak value of the dissociative electron attachment cross section is 0.16 \AA^2 at 5.2 eV. The angular distribution of fragments changes its character considerably with varying electron energies and reveals different symmetries of the involved resonant states.

DOI: [10.1103/PhysRevA.99.052705](https://doi.org/10.1103/PhysRevA.99.052705)**I. INTRODUCTION**

In recent years, the electron collisions with and the anion chemistry of nitriles have been attracting attention due to their possible role in astrochemistry and planetary atmospheric chemistry [1]. The motivation originates primarily from two sources. The first is the fact that the linear anions CN^- , C_3N^- , and C_5N^- are among the few molecular anions detected in outer space. The second source of interest is the chemistry of Titan's atmosphere, where the Cassini-Huygens mission detected anions with a wide range of masses [2,3], the CN^- being the most abundant anion.

One of the possible neutral precursors for the CN^- anion in these environments is cyanogen (NCCN). It has been directly identified in Titan's upper atmosphere [4]. It has also been long speculated that it is abundant in interstellar clouds [5,6]; however, its direct spectroscopic identification is impossible due to the lack of dipole moment. Recently, very firm evidence of its presence in dense clouds L483 and TMC-1 has been provided by the detection of protonated cyanogen [7] and its polar isomer isocyanogen [8]. The authors of these observations supported the ideas of high abundance of NCCN in molecular clouds and pointed out an almost complete lack of data for the key reactions of this molecule.

Here we focus on the dissociative electron attachment (DEA)



Even though there exist two studies that probed the relative ion yield [9,10] and even the kinetic energy and angular distributions of the CN^- fragments [10], we are not aware of any absolute cross-section measurements. This is in contrast to a number of linear molecules for which astroinspired quantitative studies exist, such as acetylene [11], diacetylene [12], hydrogen cyanide [13], or cyanoacetylene HC_3N [14]. The resonances (transient anion states) that may present the states leading to DEA were probed experimentally by electron

transmission spectroscopy [15] and theoretically by scattering calculations [16]. Also relevant is the calculation of the integral scattering cross section by the Schwinger variational method [17].

In the present paper we report the absolute cross section for the process (1) and provide the kinematic details of this reaction by using velocity map imaging. This has been enabled by the construction of an experimental setup, which is presented in detail. Apart from providing the quantitative data that may be used in modeling the astrophysical environments, the results provide insight into the dynamics and mechanisms of the DEA in cyanogen.

II. EXPERIMENT

The present setup is based on the trochoidal electron spectrometer, constructed and operated for many years at the University of Fribourg, Switzerland. The apparatus has evolved considerably over the time. In its original form, it was a magnetically collimated electron energy loss spectrometer [18]. Upon adding an ion-source lens, it served as an anion-molecule collision associative electron detachment spectrometer [19]. Later, the ion lens was discarded and the spectrometer was modified for measuring absolute DEA cross sections, either by a total ion collection method [20] or by a quantitative time-of-flight technique [11]. In this form, the spectrometer was transferred to Prague in 2016. Here we describe in detail its most recent modification.

A. Arrangement

The schematic of the current arrangement is shown in Fig. 1. A pair of magnetic coils mounted outside the vacuum chamber producing around 80-G uniform magnetic field is used to collimate the electron beam. The beam is produced in a trochoidal electron monochromator, which stayed in its original form [18] during all the previous setup modifications. The electron beam is pulsed (300-ns width at 40-kHz repetition rate). The molecular beam, directed towards the detector, is produced by passing the sample gas with a controllable flow rate through a nozzle of 500- μm diameter. The electron

^{*}pamir.nag@gmail.com[†]juraj.fedor@jh-inst.cas.cz

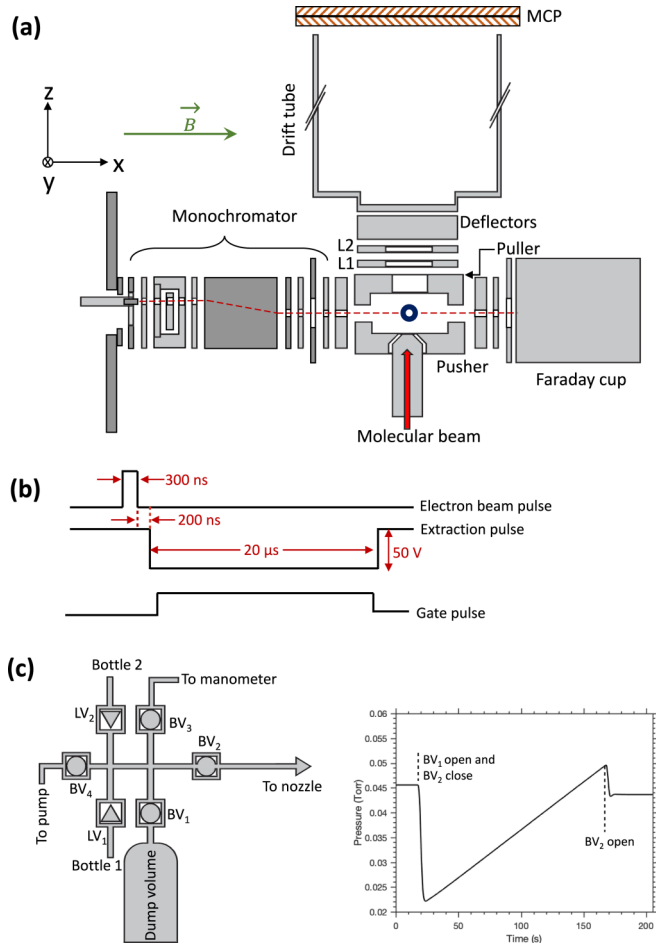


FIG. 1. (a) Scheme of the experimental setup. (b) Voltage pulsing scheme. (c) Shown on the left is the scheme of the inlet system and on the right is time dependence of the Baratron pressure during the flow measurement (the experimental curve is for NCCN).

and molecular beams interact in a field-free condition at the center of the first two electrodes of the ion optics assembly. The electron current is recorded in a Faraday cup mounted after the collision region. The Faraday cup is actually the former trochoidal analyzer, short-circuited and kept at +25 V, and the electron current is monitored using a Keithley 2700 electrometer.

The anions produced are extracted 200 ns after the electron beam has passed from the interaction region by applying a -50 -V potential on the first electrode (pusher plate) of the spectrometer. The second electrode (puller), placed 6 mm away from the pusher plate, has a circular opening of 8-mm diameter and was kept at the ground potential. The next two electrodes, called lens 1 and lens 2 (L1 and L2), are of 19-mm diameter and have 13-mm holes. During the current experiment an electric field around 140 V/mm was applied between the puller-L1 and L1-L2 electrodes. A deflector was placed next to the L2 electrode to be able to steer the Newton sphere along the y direction in order to compensate for drift induced by the magnetic field. A 70-V/mm electric field was applied between L2 and the deflectors. A field-free drift tube of 118-mm length is placed after the deflectors and again a 70-V/mm field was applied between the deflectors and

the drift tube. The drift tube has a 13-mm-diam opening towards deflectors and 37-mm-diam opening near the detector. The variable diameter is necessary due to the space constraint of the monochromator end plate. The lens assembly is manufactured from molybdenum and is actually based on the electrodes originally used in the ion lens system of the associative detachment spectrometer [19].

B. Detection scheme

A time- and position-sensitive detector with 40-mm active diameter was used. The detector consists of a pair of microchannel plates (MCPs) in chevron configuration, placed at about 5 mm away from the drift tube, and an LC delay-line hexanode [21], placed outside the vacuum chamber. The total distance between the interaction region and the detector is 170 mm. The front plate of the MCP was kept at 500 V and a 2400-V potential difference across the MCPs was applied. Two different sets of data acquisition systems were used for velocity map imaging and absolute cross-section measurement purposes. The (x, y) position of each detected ion is measured from the three pairs of delay-line signals, whereas the MCP signal is used to trigger the data acquisition system as well as determine the time of flight (TOF) of the ions. A nuclear instrumentation module (NIM) logic pulse at a time identical to that of the electron gun pulse was generated and used as the time zero marker for the TOF measurement purpose. The outputs of the delay-line anode and MCP were at first amplified using a fast timing amplifier and then fed to an eight-channel NIM standard constant fraction discriminator (CFD) to produce NIM logic pulses. The pulsed voltage applied on the pusher plate interferes with all the signals and produces a noise pickup during the switching time. To avoid any false signal from getting recorded, a gate pulse with proper timing [as shown in Fig. 1(b)] was applied to the CFD and any signal not coinciding with the gate pulse was rejected by the CFD. All the CFD outputs and the time zero signal were finally applied to a time to digital converter mounted on a dedicated computer, where the (x, y) position and time of flight of each detected ion were determined and stored in a listmode file. The CoboldPC software was used for acquisition and further analysis.

C. Velocity map imaging

The velocity mapping condition ensures that ions with different starting positions but with the same momentum vectors will hit the detector at the same spot. Their arrival time is influenced by the z component of their initial velocity. The typical spread of the arrival times (FWHM of the time-of-flight peak) of CN^- ions around the 5.5-eV incident electron energy is about 100 ns. Due to the use of the delay-line detector, we can reconstruct the Newton sphere in the coordinate representation (x, y, z) . The (x, y) coordinate for each ion is directly recorded and the z coordinate is reflected in the arrival time. To extract z , we use the cylindrical symmetry which is imposed by the electron beam parallel to the detector. The radius of each Newton sphere in the y direction thus has to be the same as in the z direction. We obtain the y radius from a 3-ns thin central slice. We define $z = 0$ at this slice. We

linearly scale the arrival times, measured from the TOF peak center, such that the z radius is equal to the y radius.

It turns out that the presence of the magnetic field necessary for the operation of the trochoidal monochromator and the geometry constraints of the existing system lead to certain distortion of the Newton sphere during its projection on the detector. This problem is described in detail in Sec. III B, where the CN^-/NCCN images are discussed. This distortion also affects the arrival times: While the forward ions with $z > 0$ after the linear scaling form an almost perfect sphere, the backward part shows a tail at large negative z , corresponding to late arrival times. We thus use only the forward part of the Newton sphere ($z > 0$) for further evaluation.

This Newton half sphere is then transformed from the coordinate scale to the kinetic energy scale as $E_{\text{kin}} = cr^2$, where r is the distance of the ion from the center. The calibration factor c is determined by measuring the O^- production of CO_2 at 8.2 eV and setting c such that the resulting kinetic energy distribution fits the distribution measured by Moradmand *et al.* [22].

The Newton half sphere constructed this way allows us to evaluate kinetic energy distributions from its various angular sections. Unless stated otherwise, we show these evaluated from a full 2π solid angle range. The angular distributions of ions are evaluated from the central slice.

D. Cross-section calibration

To determine the absolute DEA cross section we use a relative flow technique [23] which compares the anion formation rate of a calibrant gas (with well-established cross section) and a sample gas for which the cross section is measured. We use the 8.2-eV band of O^-/CO_2 with an energy-integrated cross section $\sigma_c = 0.56 \times 10^{-22} \text{ eV } \text{\AA}^2$ [11,24,25] for calibration. The sample gas energy-integrated cross section σ_s is given as

$$\sigma_s = \sigma_c \frac{N_s I_c F_c}{N_c I_s F_s} \sqrt{\frac{M_c K_c}{M_s K_s}}. \quad (2)$$

The variables with subscript c and s represent the corresponding quantities for the calibrant (O^-/CO_2) and the sample (CN^-/NCCN) compounds, respectively. Here N is the energy-integrated anion formation count rate (here all the ions in the time-of-flight peak are counted, not only the central slice); I , F , and M are the electron beam current, molecular flow rate, and molecular mass, respectively; and the K 's are transmission of the ions and detection efficiency of the spectrometer. Since we see on the image that we collect all the ions, the transmission coefficient is certainly 1. The detection efficiency of anions may depend on their impact velocity on the MCP front plane. We have checked that we are operating in the saturation regime, and thus consider $K_c/K_s = 1$.

The molecular flow rate F is controlled by variable leak valves LV_1 or LV_2 . A capacitance manometer (MKS Baratron type 690A) is attached in between the nozzle and the low-pressure side of the leak valve. When the gas flows freely through the nozzle the pressure remains constant with time. The flow rate is measured by first suddenly decreasing the pressure on the low-pressure side of the leak valve (by opening a ball valve BV_1 to a dump volume) and

simultaneously stopping the flow through the nozzle (by shutting the ball valve BV_2 leading to it). The pressure in the Baratron increases nearly exactly linearly with time and the flow rate is determined from this pressure increase.

E. Error budget and verification of the calibration

The statistical variation of the cross section evaluated by the method described above had a scatter of $\pm 7\%$ (standard deviation evaluated from ten calibration runs). The pressure stability during one measurement was within $\pm 3\%$ and the electron current stability was in a similar order.

A possible systematic error in the relative flow technique stems from the fact that the molecular beam profile can depend on the pressure. To ensure equal profiles of the beam for various compounds, it is recommended to adjust the driving pressures behind the nozzle such that their mean molecular mean free paths are equal [26]. The mean free path depends on the gas kinetic molecular diameter, which is difficult to evaluate. Nonetheless, using a nozzle basically identical to the present one, Allan has investigated the dependence of the evaluated cross section on the sample to the calibrant gas pressure ratio [26] (in an elastic electron scattering experiment, with a helium calibrant gas). It turns out that the sensitivity is low: Changing the pressure ratio by a factor of 2 results in the change of the cross section within $\pm 5\%$.

Combining the above-listed uncertainties with the error bar of the calibrant gas cross section (estimated to be $\pm 10\%$, given by the scatter of the absolute data from Refs. [11,24,25]), we estimate the present cross-section values to be accurate within $\pm 15\%$. We have verified the calibration procedure by measuring the cross sections for a number of compounds known from the literature. These were N_2O [24], hexafluoropropylene oxide [27], and HCOOH [28]. In all these cases, the present values agreed with the literature values within a few percent.

F. Experimental conditions and procedure

The typical electron current used in the present experiments was 10 nA in the cw mode. The electron energy scale was calibrated using the 4.4-eV resonance in the O^-/CO_2 cross section. The shape of this band was also used to determine the electron beam resolution, which was around 250-meV FWHM.

First, the CN^-/NCCN cross section was measured by the method described above. The typical timescale for one acquisition of the NCCC/CO_2 pair was 2 h; ten pairs of measurements were taken. Later, we recoded the images at several fixed electron energies with good spatial statistics. The typical timescale for one such acquisition was 5 h.

G. The NCCN sample

Cyanogen was prepared by a modified literature procedure [29] in which an aqueous solution of potassium cyanide (11.6 g in 50 ml of water) was poured onto 22.3 g of copper(II) sulphate pentahydrate powder at a temperature rising from 50°C to 90°C . Evolving cyanogen was passed through a Dimroth condenser to get rid of water vapors and captured in a flask cooled down by a mixture of dry ice and acetone to

a temperature of -78°C . Subsequently, the frozen cyanogen was resublimed in vacuum (less than 1 mbar) into a lecture bottle. Its purity was checked by electron-impact mass spectrometry and determined to be better than 98%.

During the measurements the lecture bottle with the sample was kept at a constant temperature of -25°C at which NCCN is liquid. This enabled handling of the vapors without any pressure reducing valve.

III. RESULTS AND DISCUSSION

A. Cross section

Figure 2 shows the cross section for the CN^- production from NCCN. The vertical marks denote the energetic thresholds yielding the ground state $\text{CN}^- (^1\Sigma^+)$ and the CN radical in the three lowest electronic states $X^2\Sigma^+ (E_{th1} = 1.56)$ eV, $A^2\Pi (E_{th2} = 2.71)$ eV, and $B^2\Sigma^+ (E_{th3} = 4.75)$ eV. The threshold values are obtained from the NC-CN dissociation energy of 5.42 eV [30], CN electron affinity of 3.86 eV [31], and CN excitation energies [32]. There is a weak DEA band with an onset at the first threshold, followed by a dominant band at 5.3 eV and a clear shoulder around 7.5 eV.

The shape of the ion yield is in excellent agreement with the early studies of Tronc and Azria [10] and Kühn *et al.* [9]; the former reported only the two strong bands, while the weak threshold band was reported by the latter group. Kühn *et al.* also provided an order of magnitude estimate of the cross-section value, based on the comparison with the SF_6^- count rate. This estimate yielded the peak cross section in the range $10\text{--}100 \text{ \AA}^2$. This is one to two orders of magnitude higher than the present value, which is not surprising, considering the very rough estimate in Ref. [9].

It may also be instructive to compare the present cross-section value with those of other astronomically detected molecules that can serve as a source of CN^- upon their interaction with free electrons. Hydrogen cyanide (HCN) has a peak cross section [13] of 0.09 \AA^2 at 1.86 eV and HC_3N has a peak cross section [14] of 0.03 \AA^2 at 5.3 eV. The present peak cross section (0.16 \AA^2) is the highest of these three compounds. It should be noted, however, that it peaks at relatively high electron energies, especially when compared

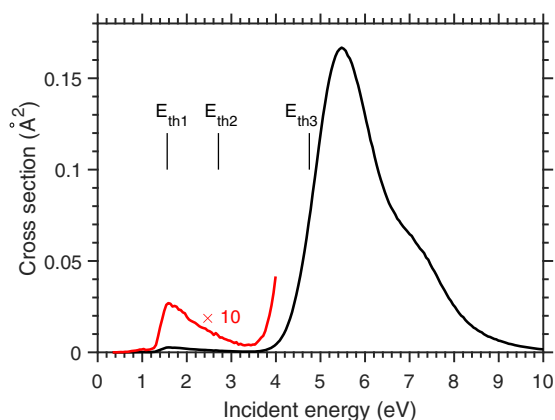


FIG. 2. DEA cross section for the formation of a CN^- fragment from $(\text{CN})_2$.

to HCN, where the DEA is efficient at threshold. The electron energy distribution in the respective environment of course has to be taken into account when judging the importance of individual neutral precursors.

B. Angular and kinetic energy distribution

Figure 3 shows the velocity slice images recorded at different electron energies. The red arrows indicate the direction of the electron beam. Since this defines the symmetry axis, ideally, the images should be top-bottom symmetric. There is a certain degree of asymmetry visible. The reason for this is the presence of the magnetic field, necessary for the operation of the trochoidal electron monochromator, which introduces an additional lateral component in the motion of ions extracted from the collision region. We correct this motion by the deflectors in the ion optics assembly. In spite of this correction, the ions with trajectories in the upper and lower halves (referring to the image plane) do not pass the VMI focusing lens systems symmetrically, which leads to a distortion of the Newton sphere. We decided not to do any symmetrization and show the raw data images.

It should be noted that the images correspond to slicing in time (3 ns). They thus do not reflect the kinetic energy distribution, since for the fast ions, a smaller fraction of their Newton sphere falls into such a time slice than for the slow ions. This effect was demonstrated by Moradmand *et al.* [22], who also showed that this can be overcome by wedged slicing: extracting a slice of a Newton sphere with a constant elevation angle, instead of a constant flight time interval. They even showed the images after such solid angle weighting. We have decided to show only the true time slicing, in order to be directly comparable to experiments that do not use delay-line detectors and thus cannot do such postprocessing of the Newton sphere. This affects only the visual image; the kinetic energy distributions are evaluated properly from the Newton forward half sphere, as described in Sec. II. It has been shown in Ref. [22] (and verified by us in the present case) that this yields the same results as wedged slicing.

The image recorded at 1.8-eV electron energy shows only a central spot, corresponding to very slow ions. This is expected, since this energy is only 0.2 eV above the DEA threshold. At energies across the main DEA band, from 5.1 to 6.1 eV, the images are similar to each other, with a constant diameter and clear preference for the perpendicular CN^- ejection. On the high-energy shoulder (7.3 and 7.7 eV), the character of the images changes, with the stronger relative intensity both in the central part and in the parallel direction.

Figure 4(a) shows the CN^- kinetic energy distributions, integrated over the whole angular range. They are in line with the qualitative description above. At 1.8-eV incident energy, the excess energy above the threshold is very low, comparable to the electron energy resolution. The CN^- distribution is thus primarily given by the velocity spread of the effusive molecular beam. A supersonic beam, such as that used to probe DEA in acetylene [33], would be necessary to probe the actual kinetic energy release in such a threshold process.

At the electron energies corresponding to the dominant DEA peak, 5.1, 5.6, and 6.1 eV, the ion kinetic energy

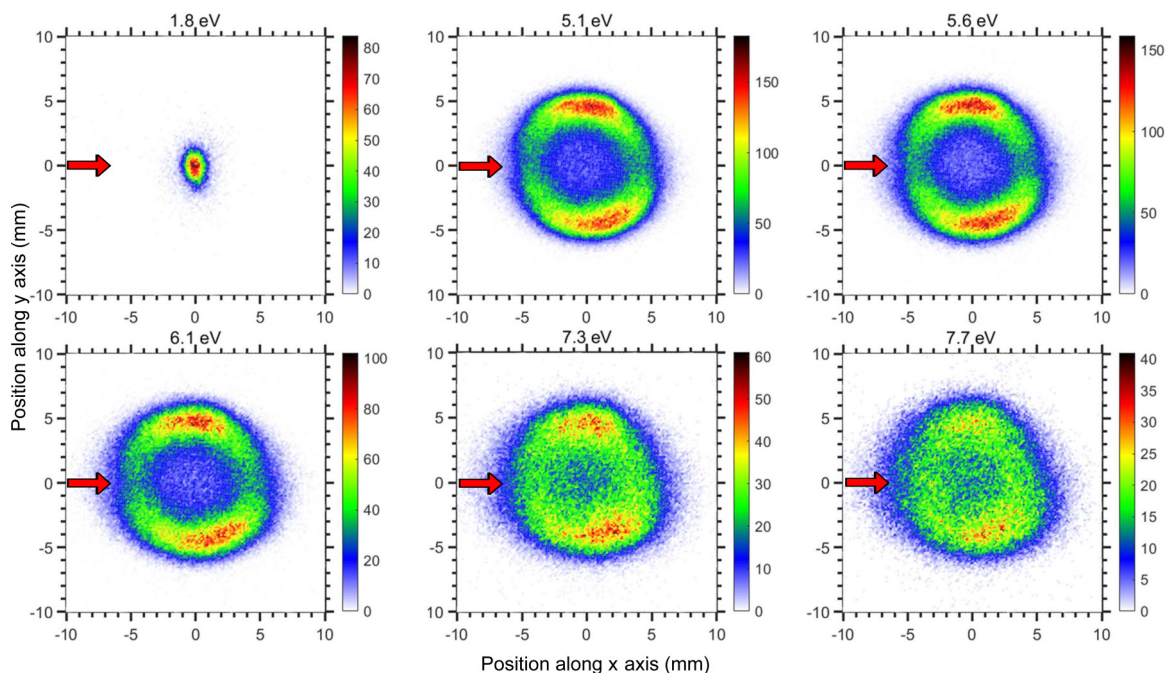


FIG. 3. Velocity slice images of CN^- ions at electron energies labeled on top of each image. The incident electron beam direction is along the $+x$ axis through the center of each image as indicated by small red arrows.

distributions have a maximum at basically identical positions, around 0.55 eV. The only difference is visible on the high-energy tail of the distribution, where the higher electron energy leads to a slightly higher abundance of fast ions. At electron energies of 7.3 and 7.7 eV, the maximum of the distribution shifts to the left and there is a clear increase of the abundance of slow fragments. Tronc and Azria [10] measured the CN^- kinetic energy distribution at a 90° angle, using a rotatable hemispherical analyzer. Figure 4(b) shows the comparison of their data with our present distribution. The agreement between the data is reasonably good; the present distribution is broader and extends to higher kinetic energies.

Angular distributions of CN^- ions are shown in Fig. 5. These distributions were evaluated in the kinetic energy range 0.2–1 eV at incident electron energies 5.1, 5.6, and 6.1 eV, and in the kinetic energy range 0.15–1.4 eV at 7.3- and 7.7-eV electron energies. At 5.1 and 5.6 eV, they show pronounced minima at 0 and 180° angles and a maximum at 90° . Due to the asymmetry described above, the second maximum is shifted to higher angles than the expected 270° . The main change with the increasing energy is that the intensity ratio of the forward to backward emitted fragments compared to those emitted at 90° is increasing in favor of the former. Here very good agreement is observed with the turntable angular distribution of Tronc and Azria at 5.5-eV electron energy [10].

C. The DEA mechanism

Let us first concentrate on the shape resonances that can be formed upon the electron interaction with NCCN. In a simple picture, these can be imagined as a temporal occupation of the molecule's virtual orbitals. The lowest four virtual orbitals of NCCN are of π_u^* , σ_u^* , π_g^* , and σ_g^* character. The

energies of the corresponding π^* resonances are determined by the electron transmission spectroscopy (ETS) [15] to be 0.58 eV (π_u^*) and 5.38 eV (π_g^*). The σ^* resonances are generally too broad to be revealed in the transmission spectra; we will thus use an empirical scaling of virtual orbital energies [35] to estimate their positions. This scaling predicts the σ_u^* resonance at 4.0 eV and the σ_g^* at 6.1 eV. It should be noted that this type of empirical correlation method was explored in depth by Sommerfeld and Weber [36] and the NCCN has shown relatively large errors; nonetheless, we will use the scaled positions only as indications.

The threshold DEA band lies considerably higher than the π_u^* resonance, which is additionally expected to be very narrow, due to its low energy. The more probable origin of this band is that it is mediated by the broad σ_u^* resonance and the signal appears only at its low-energy tail. Due to the expected large width of this resonance, it will have a very high autodetachment rate and this rate will also increase with the electron energy [37]. This is one of the reasons why it yields the DEA signal only at the threshold. The second possible reason is a considerable polarizability of cyanogen of 5.02 \AA^3 [38]. This will cause a long-range interaction between the electron and the target molecule. Due to the coupling with the broad σ_u^* resonance, such an interaction can dramatically increase the dissociative cross section [39–41].

The main DEA band centered around 5.3 eV has several surprising characteristics. One concerns the energy partitioning and one the angular distributions. The band's center overlaps perfectly with the ETS position of the π_g^* resonance. These resonant states correlate with the $\text{CN}^-(^1\Sigma^+) + \text{CN}(^2\Pi)$ asymptotic limit at 2.75 eV (E_{th2}). If all the excess energy went into the kinetic energy of the fragments, the CN^- kinetic energy would be 1.18 eV at 5.1 electron energy and

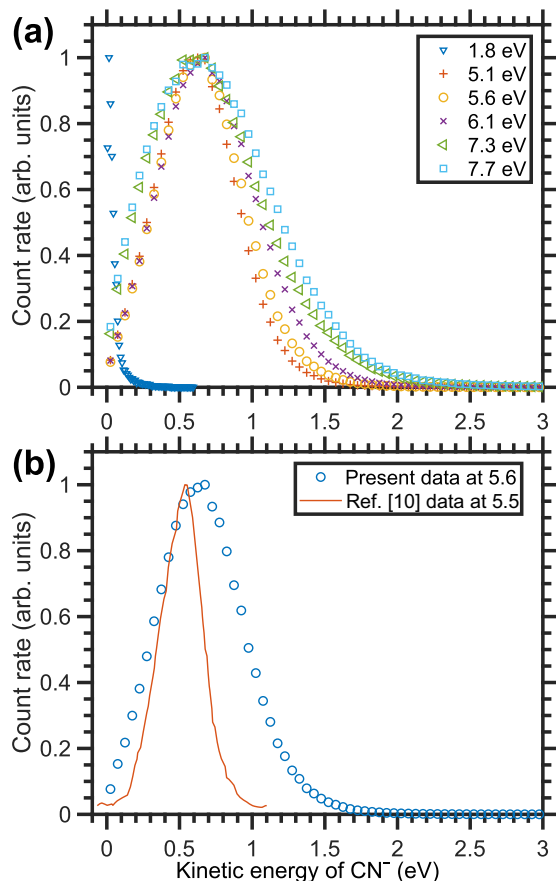


FIG. 4. Kinetic energy distributions of the CN^- ions for a number of incident electron energies (a) angle integrated in the full angular range and (b) angle integrated in the $90^\circ \pm 20^\circ$ range and compared with the 90° data of Tronc and Azria [10].

1.67 eV at 6.1 electron energy. Instead, the kinetic energy distributions in Fig. 4 peak around 0.55 eV and this peak value does not change with the electron energy in this energy range. This suggests that the fragments are produced with a considerable amount of internal energy which is left in either the vibrational or rotational excitation of the fragments.

The second puzzle concerns the angular distribution. The linear symmetric structure of the target molecule may suggest the use of a simple prescription for the angular distribution developed for the diatomic molecules by O'Malley and Taylor [34]. Even though it is a pioneering work dating back to 1968, it is still being used often for the data interpretation of the VMI experiments [42,43], especially in the simplified formalism developed by Tronc *et al.* [44] and Azria *et al.* [45]. It provides a prescription for the angular distributions for a given symmetry of the neutral state, a given symmetry of the resonant state, and a given partial wave component of the incoming electron. Figure 5(b) shows the distribution obtained from that formalism, assuming the $^1\Sigma_g^+$ neutral state and Π_g resonant state. According to the selection rules [44], only the partial waves with $l = 2$ (*d* wave), $l = 4$ (*g* wave), or higher even l couple to this resonant state. The contribution from each partial wave is proportional to spherical harmonics $Y_{l\mu}$, where μ is the change of the axial angular momentum upon the resonance formation, in this case $\mu = 1$. Independent of

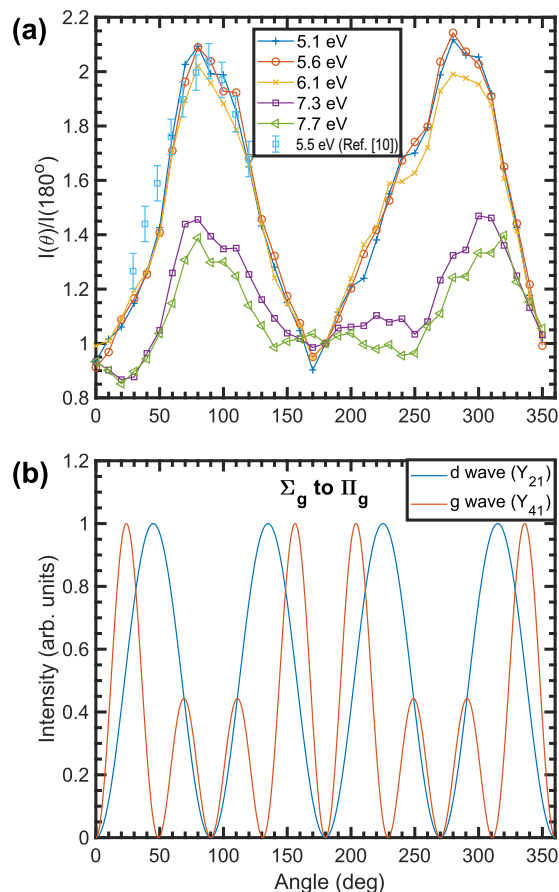


FIG. 5. (a) Angular distributions of the CN^- ions at the electron energies defined in the legend. (b) Angular distributions calculated from the model of O'Malley and Taylor [34] assuming the single π_g^* resonance for two different allowed partial waves of the incoming electron.

the partial wave, the theoretical distributions exhibit behavior very different from the experimental one.

At the same time it should be said that this is not really surprising. Cyanogen is not a homonuclear diatomic molecule. It has been beautifully demonstrated for acetylene that if there is a distortion of the linear structure involved during the DEA dynamics, the angular distribution can change dramatically when compared to a model where no bending is involved. The same is true for the 8.2-eV resonance in CO_2 , where the attachment amplitude could be made to resemble the measured fragment angular distribution by averaging the calculation over bent geometries of the transient anion [46]. That might be happening also in the present case. The high internal energy content of the fragments concluded from the energy distribution supports this mechanism. Another option is that the occurrence of the 5.3 DEA band at the energy of the π_g^* resonance is fortuitous and in reality it is mediated by a core-excited resonance of a different symmetry, an option that has arisen also in diacetylene [47] or cyanoacetylene [14]. Here it should be just noted that the fragments are certainly not produced in the asymptotic limit E_{th3} , since the low excess energy associated with this limit (0.35 eV at 5.1-eV electron energy) cannot account for the observed CN^- kinetic energies. Also, there is a possibility that the two σ^* states play

a role in the dissociation mechanism (e.g., via their vibronic coupling to the π_g^* resonance). They asymptotically correlate with the E_{th1} limit [15]. In this case the difference between the maximal and the observed CN^- kinetic energy would be even larger than if the fragments were produced in E_{th2} which correlates with the π_g^* resonance. A proper calculation that accounts for the multidimensional dissociation dynamics, such as that recently done for a number of target molecules [33,48,49], is needed to answer this question.

The same is true for the interpretation of changes that appear at higher incident energies, 7.1 and 7.7 eV. These are (i) increased abundance of slow fragments (however, without clearly discernible peak in the kinetic energy distribution) and (ii) much higher abundance of the forward or backward emitted fragments. Open questions are whether and how the probable presence of a broad σ_g^* resonance in this energy range influences these observations.

IV. CONCLUSION

We have considerably modified an existing quantitative DEA time-of-flight spectrometer such that it now incorporates

the velocity map imaging while simultaneously keeping the ability to measure absolute cross sections. We have used it to determine the DEA cross section for the CN^- production in cyanogen. The cross section reaches values that are higher than those for other possible sources of CN^- via electron impact in outer space or planetary atmospheres. The kinetic energy and angular distributions extracted from the velocity map images are in very good agreement with the data of Tronc and Azria [10] obtained by a rotatable analyzer technique. The present results that reveal the full angular range of the fragment distribution at a number of incident electron energies shed light on the DEA mechanism; however, at the same time they reveal several open questions regarding the actual dissociation dynamics and energy partitioning. We believe that our findings will inspire advanced theoretical treatment of this problem.

ACKNOWLEDGMENTS

This work was part of Project No. 17-04844S of the Czech Science Foundation. We thank our colleague Roman Čurík for fruitful discussions.

-
- [1] T. J. Millar, C. Walsh, and T. A. Field, *Chem. Rev.* **117**, 1765 (2017).
- [2] A. J. Coates, F. J. Crary, G. R. Lewis, D. T. Young, J. H. Waite, and E. C. Sittler, *Geophys. Res. Lett.* **34**, L22103 (2007).
- [3] V. Vuitton, P. Lavvas, R. V. Yelle, M. Galand, A. Wellbrock, G. R. Lewis, A. J. Coates, and J.-E. Wahlund, *Planet. Space Sci.* **57**, 1558 (2009).
- [4] V. G. Kunde, A. C. Aikin, R. A. Hanel, D. E. Jennings, W. C. Maguire, and R. E. Samuelson, *Nature (London)* **292**, 686 (1981).
- [5] R. Kolos and Z. R. Grabowski, *Astrophys. Space Sci.* **271**, 65 (2000).
- [6] S. Petrie, T. J. Millar, and A. J. Markwick, *Mon. Not. R. Astron. Soc.* **341**, 609 (2003).
- [7] M. Agúndez, J. Cernicharo, P. de Vicente *et al.*, *Astron. Astrophys.* **579**, L10 (2015).
- [8] M. Agundez, N. Marcelino, and J. Cernicharo, *Astrophys. J. Lett.* **861**, L22 (2018).
- [9] A. Kühn, H.-P. Fenzlaff, and E. Illenberger, *Chem. Phys. Lett.* **135**, 335 (1987).
- [10] M. Tronc and R. Azria, *Chem. Phys. Lett.* **85**, 345 (1982).
- [11] O. May, J. Fedor, and M. Allan, *Phys. Rev. A* **80**, 012706 (2009).
- [12] O. May, J. Fedor, B. C. Ibănescu, and M. Allan, *Phys. Rev. A* **77**, 040701(R) (2008).
- [13] O. May, D. Kubala, and M. Allan, *Phys. Rev. A* **82**, 010701(R) (2010).
- [14] M. Ranković, P. Nag, M. Zawadzki, L. Ballauf, J. Žabka, M. Poláček, J. Kočišek, and J. Fedor, *Phys. Rev. A* **98**, 052708 (2018).
- [15] L. Ng, V. Balanji, and K. D. Jordan, *Chem. Phys. Lett.* **101**, 171 (1983).
- [16] F. Sebastianelli, F. Carelli, and F. Gianturco, *Chem. Phys.* **398**, 199 (2012).
- [17] S. E. Michelin, A. S. Falck, K. T. Mazon, J. J. Piacentini, M. A. Scopel, L. S. S. da Silva, H. L. Oliveira, M. M. Fujimoto, I. Iga, and M.-T. Lee, *Phys. Rev. A* **74**, 022702 (2006).
- [18] M. Allan, *J. Electron Spectrosc. Relat. Phenom.* **48**, 219 (1989).
- [19] S. Živanov, M. Allan, M. Čížek, J. Horáček, F. A. U. Thiel, and H. Hotop, *Phys. Rev. Lett.* **89**, 073201 (2002).
- [20] J. Fedor, O. May, and M. Allan, *Phys. Rev. A* **78**, 032701 (2008).
- [21] O. Jagutzki, A. Czasch, and S. Schössler, in *Advanced Photon Counting Techniques VII*, edited by M. A. Itzler, SPIE Proc. Vol. 8727 (SPIE, Bellingham, 2013).
- [22] A. Moradmand, D. S. Slaughter, A. L. Landers, and M. Fogle, *Phys. Rev. A* **88**, 022711 (2013).
- [23] E. Krishnakumar and S. K. Srivastava, *J. Phys. B* **21**, 1055 (1988).
- [24] D. Rapp and D. D. Briglia, *J. Chem. Phys.* **43**, 1480 (1965).
- [25] O. J. Orient and S. K. Srivastava, *Chem. Phys. Lett.* **96**, 681 (1983).
- [26] M. Allan, *J. Phys. B* **40**, 3531 (2007).
- [27] M. Zawadzki, A. Chachereau, J. Kočišek, C. M. Franck, and J. Fedor, *J. Chem. Phys.* **149**, 204305 (2018).
- [28] R. Janečková, D. Kubala, O. May, J. Fedor, and M. Allan, *Phys. Rev. Lett.* **111**, 213201 (2013).
- [29] G. Brauer, *Handbook of Preparative Inorganic Chemistry*, 2nd ed. (Academic, New York, 1963), Vol. I.
- [30] W. Tsang, S. H. Bauer, and M. Cowperthwaite, *J. Chem. Phys.* **36**, 1768 (1962).
- [31] S. E. Bradforth, E. H. Kim, D. W. Arnold, and D. M. Neumark, *J. Chem. Phys.* **98**, 800 (1993).
- [32] G. Herzberg, *Molecular Spectra and Molecular Structure I: Spectra of Diatomic Molecules* (Van Nostrand, Princeton, 1950).
- [33] M. Fogle, D. J. Haxton, A. L. Landers, A. E. Orel, and T. N. Rescigno, *Phys. Rev. A* **90**, 042712 (2014).

- [34] T. F. O'Malley and H. S. Taylor, *Phys. Rev.* **176**, 207 (1968).
- [35] D. Chen and G. A. Gallup, *J. Chem. Phys.* **93**, 8893 (1990).
- [36] T. Sommerfeld and R. J. Weber, *J. Phys. Chem. A* **115**, 6675 (2011).
- [37] I. I. Fabrikant, S. Eden, N. J. Mason, and J. Fedor, *Adv. At. Mol. Opt. Phys.* **66**, 545 (2017).
- [38] R. Kobayashi, H. Koch, and P. Jorgensen, *J. Chem. Phys.* **101**, 4956 (1994).
- [39] I. I. Fabrikant, *J. Phys. B* **49**, 222005 (2016).
- [40] M. Zawadzki, M. Čížek, K. Houfek, R. Čurík, M. Ferus, S. Civiš, J. Kočíšek, and J. Fedor, *Phys. Rev. Lett.* **121**, 143402 (2018).
- [41] M. Allan, M. Lacko, P. Papp, Š. Matejčík, M. Zlatar, I. I. Fabrikant, J. Kočíšek, and J. Fedor, *Phys. Chem. Chem. Phys.* **20**, 11692 (2018).
- [42] K. Gope, V. Tadsare, V. S. Prabhudesai, and E. Krishnakumar, *Eur. Phys. J. D* **71**, 323 (2017).
- [43] I. Jana and D. Nandi, *Phys. Rev. A* **97**, 042706 (2018).
- [44] M. Tronc, F. Fiqued-Fayard, C. Schermann, and R. I. Hall, *J. Phys. B* **10**, 305 (1970).
- [45] R. Azria, Y. L. Coat, G. Lefevre, and D. Simon, *J. Phys. B* **12**, 679 (1979).
- [46] D. S. Slaughter, H. Adaniya, T. N. Rescigno, D. J. Haxton, A. E. Orel, C. W. McCurdy, and A. Belkacem, *J. Phys. B* **44**, 205203 (2011).
- [47] M. Allan, O. May, J. Fedor, B. C. Ibănescu, and L. Andric, *Phys. Rev. A* **83**, 052701 (2011).
- [48] T. N. Rescigno, C. S. Trevisan, A. E. Orel, D. S. Slaughter, H. Adaniya, A. Belkacem, M. Weyland, A. Dorn, and C. W. McCurdy, *Phys. Rev. A* **93**, 052704 (2016).
- [49] D. S. Slaughter, A. Belkacem, C. W. McCurdy, T. N. Rescigno, and D. J. Haxton, *J. Phys. B* **49**, 222001 (2016).